

Journal of  
**Applied  
Crystallography**

ISSN 0021-8898

Editor: **Gernot Kosterz**

## **High-resolution three-dimensional mapping of individual grains in polycrystals by topotomography**

**Wolfgang Ludwig, Erik Mejdal Lauridsen, Soeren Schmidt, Henning Friis Poulsen and José Baruchel**

Copyright © International Union of Crystallography

Author(s) of this paper may load this reprint on their own web site or institutional repository provided that this cover page is retained. Reproduction of this article or its storage in electronic databases other than as specified above is not permitted without prior permission in writing from the IUCr.

For further information see <http://journals.iucr.org/services/authorrights.html>

# High-resolution three-dimensional mapping of individual grains in polycrystals by topotomography

Wolfgang Ludwig,<sup>a,b\*</sup> Erik Mejdal Lauridsen,<sup>c</sup> Soeren Schmidt,<sup>c</sup> Henning Friis Poulsen<sup>c</sup> and José Baruchel<sup>b</sup>

<sup>a</sup>Laboratoire MATEIS, UMR 5510 CNRS, INSA-Lyon, France, <sup>b</sup>European Synchrotron Radiation Facility, 6 rue Jules Horowitz, BP 220, 38043 Grenoble CEDEX, France, and <sup>c</sup>Centre for Fundamental Research: Metal Structures in Four Dimensions, Risø National Laboratory, Roskilde, Denmark. Correspondence e-mail: wolfgang.ludwig@insa-lyon.fr

By orienting a crystal grain with its diffraction vector along the sample rotation axis, it is possible to use powerful tomographic and topographic imaging techniques to reconstruct the three-dimensional grain shape inside a polycrystalline sample. The acquisition and reconstruction can be performed from projection images with the detector positioned either in the diffracted-beam or in the direct-beam position. In the first case, the projection data consist of a series of integrated, monochromatic beam X-ray diffraction topographs of the grain under investigation. In the second case, the corresponding diffraction contrast in the transmitted beam may be interpreted as an additional contribution to the X-ray attenuation coefficient of the material. This latter variant is restricted to grains with small orientation spread but offers the possibility to characterize simultaneously the three-dimensional grain shape and the absorption microstructure of the surrounding sample material. The contrast mechanism is sensitive to local strain fields and can, in certain cases, reveal details of the grain microstructure, such as the presence of second-phase inclusions. The methodology is successfully demonstrated on an aluminium polycrystal, with a resulting three-dimensional mapping accuracy better than 7  $\mu\text{m}$ . The possibilities and limitations of the technique are listed and its performance relative to other three-dimensional mapping techniques is discussed.

© 2007 International Union of Crystallography  
Printed in Singapore – all rights reserved

## 1. Introduction

It has been demonstrated that the principles of X-ray diffraction topography and X-ray computed tomography can be combined and may provide insight into the three-dimensional dislocation structure in nearly perfect single crystals (Ludwig *et al.*, 2001). The underlying imaging concept has recently been transferred to transmission electron microscopy (TEM) (Barnard *et al.*, 2006) and the three-dimensional arrangement of dislocation in a thin TEM specimen has been imaged with considerable gain in spatial resolution.

In this article, an extension of the initial X-ray topotomographic imaging technique to the case of undeformed polycrystalline materials is presented. More specifically, one individual grain in the bulk of an aluminium polycrystal has been mapped in three dimensions. With a grain orientation spread of the order of  $0.05^\circ$ , the diffraction from this kind of crystal is in the transition regime between kinematical and dynamical theory of X-ray diffraction. As will be demonstrated, one may observe image contrast related to the presence of long-range strain fields, known as the 'direct image' in X-ray diffraction imaging (Tanner, 1976). These

local contrasts superpose on a slowly varying two-dimensional intensity distribution, reflecting the integrated reflectivity of the grain matrix for the selected imaging conditions.

Two different data acquisition schemes can be used: (i) recording of grain projections in the diffracted beam and (ii) recording of projections in the direct, transmitted beam. As will be shown and discussed in the following sections, the former case extends the range of applicability towards samples with a somewhat larger mosaic spread, while the latter case simultaneously provides a grain map and all the information obtainable from a conventional three-dimensional absorption or phase contrast tomogram of the grain and its surroundings.

Compared with other nondestructive three-dimensional grain-mapping techniques, such as sequential section topography (Kvardakov *et al.*, 2007), three-dimensional X-ray diffraction (3DXRD) microscopy (Poulsen, 2004) or differential aperture X-ray microscopy (DAXM) (Larson *et al.*, 2002), topotomographic grain imaging is unique in offering a high-spatial-resolution grain map and a simultaneous characterization of the absorption microstructure. The technique can be easily implemented at any synchrotron beamline providing a tomographic imaging setup.

## 2. Principle

Fig. 1(c) shows the principal elements of the acquisition setup and geometry used for combined topographic and tomographic image acquisition. As in conventional absorption tomography, the sample has to be centred on the rotation axis ( $\omega$ ) by means of the  $X$  and  $Y$  translations on top of the rotation table. In addition, the grain of interest has to be aligned in such a way that the diffraction condition is maintained for any  $\omega$  position during acquisition of a tomographic scan. For this, the diffraction vector  $\mathbf{G}$  associated with the selected reflection must be aligned parallel to the rotation axis. The rotation axis itself is inclined by  $(90 - \theta_{\text{Bragg}}^\circ)$  with respect to the incoming beam (where  $\theta_{\text{Bragg}}$  is the Bragg angle of the reflection). In order to enable this configuration three additional motorized degrees of freedom are required with respect to a conventional tomographic imaging setup: a base tilt cradle  $T0$  below the rotation axis (rotation around an axis perpendicular to the beam) and a goniometer head ( $X$ ,  $Y$ ,  $T1$ ,  $T2$ ) on top of the rotation table. The mechanics have to be assembled in such a way that the base tilt and goniometer head centre of rotation coincide at a point located on the axis of the rotation table.

Owing to dispersion effects (Servidori *et al.*, 2001) and orientation gradients inside the grain of interest, a static exposure will only show part of the diffracting grain volume. Therefore, a small, integrating base tilt rocking movement covering the orientation spread of the grain is performed during each exposure. The axis of this movement is perpendicular to the diffraction plane, irrespective of the current  $\omega$  setting (Fig. 1c). In order to limit the possible degradation of the spatial resolution by the geometrical blurring induced by this integrating base tilt movement, the grain of interest has to be positioned in the centre of rotation of the base tilt cradle. Since this positioning can be performed with an accuracy of at least 100  $\mu\text{m}$  (grain size), the contribution of this geometrical blurring can typically be neglected.

Two basic acquisition schemes are possible: (i) recording of grain projections in the diffracted beam and/or (ii) recording

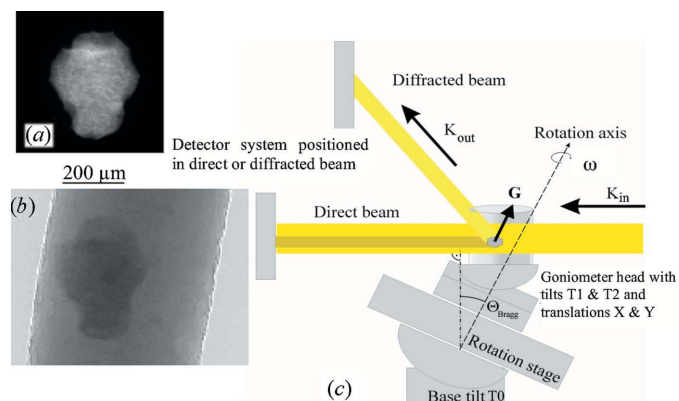


**Figure 1**

(a) Integrated diffraction topograph acquired in the diffracted beam. (b) Integrated projection image acquired in the direct beam. (c) Topotomography setup. The scattering vector ( $\mathbf{G}$ ) of a suitable reflection is aligned parallel to the rotation axis of the tomographic setup by means of tilts  $T1$  and  $T2$ . Projection images are recorded either in the direct or in the diffracted beam, while the sample is turned stepwise in  $\omega$  through  $360^\circ$ . Each image is integrated over a small rocking movement of base tilt  $T0$ .

of grain projections in the transmitted beam. In the first case the intensity distribution in the diffracted beam can be approximated to a projection of the grain volume along the direction of the diffracted beam. In the second case, the projection direction is parallel to the incoming beam and the diffracting grain gives rise to an additional contribution  $\mu^{\text{diffr}}(r)$  (coherent scattering) to the local attenuation coefficient  $\mu^{\text{eff}}(r) = \mu^{\text{abs}}(r) + \mu^{\text{diffr}}(r)$ . Neglecting for the moment effects from the dynamical theory of X-ray diffraction, the intensity decay along the transmitted beam can be approximated by the exponential function

$$I(x, y) = I_0(x, y) \exp\left[-\int \mu^{\text{eff}}(r) dz\right]. \quad (1)$$

Logarithmic subtraction of the incoming-beam profile yields in this second case projections of the unknown three-dimensional attenuation coefficient distribution

$$\int \mu^{\text{eff}}(r) dz = -\ln I(x, y)/I_0(x, y), \quad (2)$$

which can then be reconstructed with the help of the same tomographic reconstruction algorithms used in conventional absorption imaging.

Since in both cases the rotation axis is not perpendicular to the beam, projections from opposite directions ( $\omega$  and  $\omega + 180^\circ$ ) are not redundant and data acquisition should be performed covering the full  $360^\circ$  rotation range in equiangular steps.

Note that the current acquisition geometry with an inclined rotation axis can be seen as a special case of cone beam tomographic acquisition geometry. As explained in more detail by Ludwig *et al.* (2001), the small beam divergence and the inclination of the rotation axis can be taken into account correctly by assignment of the actual source-to-sample distance  $D$  (145 m in the case of ID19) and a (virtual) vertical detector offset of  $\pm D \tan \theta_{\text{Bragg}}$ . This allows one to use fast analytical tomographic reconstruction algorithms established for the cone beam case without any change. As a consequence, the data reconstruction is straightforward and relatively fast (typical reconstruction times are of the order of one hour for a  $1024^3$  voxel data set).

## 3. Results

The experiments presented in this paper were performed on the ID19 high-resolution imaging beamline of the European Synchrotron Radiation Facility, France (ESRF). Employing a narrow-bandwidth ( $\Delta E/E \simeq 10^{-4}$ ) Si 111 double-crystal monochromator in connection with a high-resolution detector system results in exposure times ranging from a second at moderate resolution (few micrometres pixel size) up to several tens of seconds at high resolution (sub-micrometre). For the current feasibility study, an effective pixel size of 2.8  $\mu\text{m}$  was chosen. The detector was placed at a distance of  $d = 50$  mm from the sample, either in-line (for gathering of data in the transmitted beam) or elevated by  $d \tan 2\theta_{\text{Bragg}}$  for gathering of diffracted-beam data. In principle one could acquire direct and diffracted-beam data simultaneously on the same detector

if  $d$  is chosen sufficiently small. In our case this configuration was not possible owing to geometric constraints.

A cylindrical sample, 550  $\mu\text{m}$  in diameter and 2 mm long, was prepared from the aluminium alloy AA1050 (99.5% Al) by means of electrical discharge machining. In order to produce a coarse-grained microstructure with a low degree of mosaic spread, the material was first cold rolled to 90% reduction, machined into the final shape and then given a 6 h recrystallization annealing at 543 K, followed by a second grain growth annealing for 4 h at 903 K. After these processing steps, the average grain size was of the order of 200  $\mu\text{m}$  and most of the grains exhibited orientation spreads below  $0.1^\circ$ . The latter information was obtained from an independent 3DXRD characterization of the sample.

A suitable 200 reflection from one of these grains was selected and aligned parallel to the rotation axis of the tomographic setup using the alignment procedure detailed in Appendix A. The integration range of the base tilt ( $T_0$ ) was set to  $\pm 0.015^\circ$ , *i.e.* slightly larger than the mosaic spread of this particular grain. The exposure time for a single integrated projection topograph was 2 s. Three different tomographic scans were recorded without changing the diffraction alignment established for an energy of 20 keV: (A) with the camera in the diffracted-beam position, (B) with the camera in the direct-beam position and (C) with the camera in the direct-beam position but with the X-ray energy detuned to 19 keV (diffraction condition no longer fulfilled). For the first scan, depicting the diffracting grain only, the grain was centred on the rotation axis and 180 projection images were acquired over a range of  $360^\circ$  in  $\omega$ . In order to achieve adequate (Fourier) space sampling of the whole specimen visible in scans B and C, these latter scans comprised 720 exposures acquired over the  $360^\circ$  range. Movies *M1* and *M2*<sup>1</sup> show the background corrected raw projection data acquired during scans A and B.

Fig. 2 shows a comparison of the reconstructed slices obtained from (a) diffracted-beam and (b) direct-beam projection data. The slices show the same sample cross section and were obtained by feeding the background-corrected projection images into a conventional filtered backprojection algorithm (cone-beam case). Fig. 2(a) clearly shows the grain outline and a distinct substructure consisting of isolated bright spots. Fig. 2(b) shows the distribution of the local attenuation coefficient in the same section of the sample; the diffraction contribution to the local attenuation coefficient leads to higher values of the attenuation coefficient in the area corresponding to the grain position. The same speckled substructure seen in Fig. 2(a) can be observed in Fig. 2(b). For comparison, Fig. 2(d) shows the corresponding sample cross section obtained from reconstruction of scan C, for which the diffraction condition was not fulfilled; superimposed on the constant attenuation background one can observe a homogeneous distribution of some weak isolated bright spots, which can be attributed to the presence of small iron-rich inclusions,

commonly encountered in material of this grade of purity. A closer analysis of the image contrasts (Fig. 2e) reveals that most of the speckled contrast visible in Fig. 2(c) coincides with the positions of the inclusions in Fig. 2(d). This local enhancement of the diffracted intensity in scans A and B is known as 'direct image' (Tanner, 1976): a well known contrast mechanism in X-ray diffraction topography. The visualization of individual dislocations in nearly perfect crystals is commonly based on this mechanism, which has also been used in the previous study to determine the three-dimensional dislocation structure in a diamond single crystal (Ludwig *et al.*, 2001). The observation that more spots are visible in the toptomographic reconstructions (Fig. 2a and c) than in the reconstruction obtained by conventional absorption contrast (Fig. 2d) indicates that inclusions below the resolution limit of the detector system can be detected. As in the case of dislocations, the technique is sensitive to the long-range strain fields associated with the presence of these defects.

A three-dimensional rendition of the grain surface, obtained from the reconstruction of scan A, is shown in Fig. 3(a) (movie *M3*). The grain has an irregularly shaped surface, containing small areas with concave curvature. After segmentation of volume B into a grain and an aluminium matrix subvolume, one may visualize the location of the grain inside the aluminium matrix (Fig. 3b). In this view the grain has been rendered fully opaque and the aluminium matrix subvolume has been cropped and rendered semi-transparent. The grain outlines and substructures determined from the

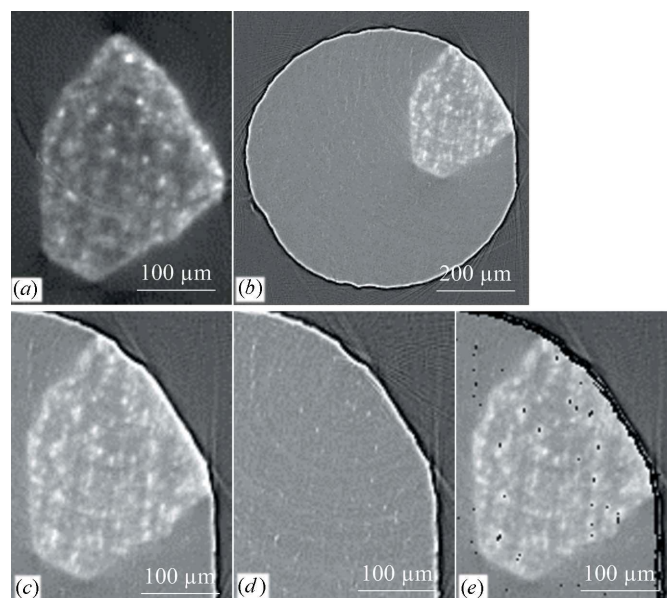


**Figure 2**  
(a) Grain slice reconstructed from diffracted-beam projections. (b) The same slice, reconstructed from direct-beam projections. (c) A zoom on the region close to the grain. (d) Absorption microstructure ( $E = 19$  keV); white spots correspond to iron-rich inclusions in this alloy. (e) Subtraction of image (d) (thresholded) from image (c) reveals that all inclusions correspond to regions with higher reconstructed attenuation coefficient values. Note the presence of diffraction contrast in regions of image (c) where no inclusions can be resolved in the corresponding absorption image (d).

<sup>1</sup> Raw projection data discussed in this paper are available from the IUCr electronic archives (reference: he5374.)

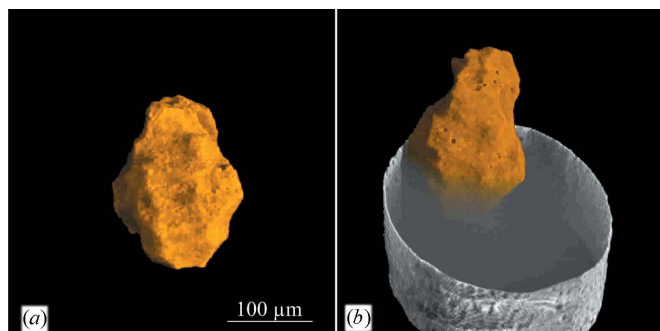


**Figure 3**  
 (a) Three-dimensional rendition of grain shape as reconstructed from diffracted-beam data. (b) Three-dimensional rendition of sample outline and grain shape as determined from direct-beam data. The data set has been segmented into a grain and an Al matrix section. The Al section has been cropped and set to transparent (the region close to the cylindrical sample outline remains visible owing to higher grey values caused by phase contrast).

direct- and the diffracted-beam reconstruction perfectly overlay. The determination of the spatial resolution by analysis of the reconstructed intensity distribution across the grain boundary is hampered by the presence of the strong diffraction contrast substructure. Fig. 4 shows a line profile of the reconstructed attenuation coefficient distribution across a nearly planar part of the grain boundary. The profile has been obtained by averaging the intensity distribution over an area of  $30 \times 50 \mu\text{m}$  on planes parallel to the grain boundary. A conservative estimate of the spatial resolution ( $7 \mu\text{m}$ ) can be obtained from the FWHM of the derivative of the line profile at the grain boundary (Fig. 4). One can conclude that the actual resolution is comparable with that offered by conventional absorption imaging and currently limited by the pixel size chosen for this demonstration experiment.

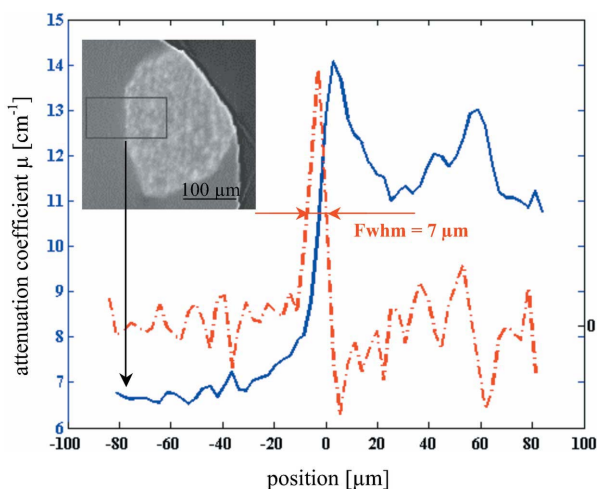


**Figure 4**  
 Estimate of the spatial resolution by analysis of the horizontal intensity profile (continuous line) and its derivative (dash-dotted line). The profile was calculated from the (vertically) averaged intensity distribution inside the box-shaped region of interest. The image represents the attenuation coefficient distribution averaged over  $30 \mu\text{m}$  in the direction perpendicular to the image plane.

## 4. Discussion

### 4.1. Comparison with other techniques

Compared with other synchrotron three-dimensional grain mapping techniques, such as 3DXRD (Poulsen, 2004) or DAXM (Larson *et al.*, 2002), where the emphasis is on simultaneous mapping of many grains, topotomography is aimed at high-spatial-resolution reconstruction of an individual grain and simultaneous reconstruction of its absorption contrast microstructure. As a scanning technique employing sub-micrometre focused beams, DAXM is interesting in terms of spatial resolution and the possibility to explore strain and orientation distribution at the sub-grain level. However, like any three-dimensional scanning technique, acquisition is slow and restricted to relatively small volumes, located close to the surface of the sample. 3DXRD on the other hand allows for fast measurements of grain structures inside bulk specimens but is currently limited in spatial resolution to about  $5 \mu\text{m}$ .

Although not yet optimized for spatial resolution, the current feasibility study demonstrated a resolution comparable with that provided by 3DXRD. However, in contrast to 3DXRD, where a compromise between concurring requirements of high spatial resolution and a large field of view (to capture a large number of diffraction spots) has to be found, in the case of topotomography one can restrict the detector field of view to the size of the sample and hence optimize the spatial resolution. In the diffracted-beam variant one may push the resolution further by zooming onto the grain under investigation. A combination of additional factors contributes to inherently higher spatial resolution. First, the particular grain alignment enables acquisition of a large number of equiangular projection images from different angles and one may therefore use well established, analytical reconstruction algorithms (filtered backprojection; Kak & Slaney 1988). In contrast, the number of exploitable projections in 3DXRD is limited to 5–20 by geometry and/or signal-to-noise considerations. Furthermore, by adjusting the sample dimensions to obtain about 20% transmission in the energy range between 10 and 30 keV, one can further optimize time and spatial resolution, which fall off rapidly when working at higher X-ray energies. Finally, the similarity to a conventional microtomographic imaging setup implies that one may take advantage of instruments that have been optimized for mechanical precision and high spatial resolution, available nowadays at most of the second- and third-generation synchrotron sources.

### 4.2. Diffracted-beam versus direct-beam acquisition

From the comparison of diffracted and direct-beam reconstruction presented in Fig. 3 one can argue that reconstructions from direct-beam data are preferable since they simultaneously give access to the microstructure visible in absorption and/or phase contrast, and allow location of the position of the diffracting grain inside the sample volume. Since the direct-beam projections do not suffer from image distortion arising from orientation components perpendicular to the diffraction plane, one may, without loss in data consis-

tency, increase the sample-to-detector distance. In the case of partially coherent illumination (typically the case at third-generation synchrotron sources) this opens the possibility to combine the topographic image contrast with phase contrast arising from Fresnel diffraction (Snigirev *et al.*, 1995; Cloetens *et al.*, 1997). Working at larger sample-to-detector distances also permits the use of sample environment (*e.g.* furnace, tensile rig): a prerequisite for future *in situ* observations. Moreover, projection images acquired in the direct beam can be corrected for nonhomogeneous beam profile and local variations in sensitivity of the detector system by the flat-field correction procedure commonly applied in absorption imaging.

One should, however, be aware that acquisition in the direct beam puts an upper limit on the acceptable grain orientation spread. Extinction contrast in the transmitted beam is related to the simultaneously diffracting grain subvolume, which in turn is inversely proportional to the grain orientation spread. In practice, the orientation spread should be of the order of  $0.1^\circ$  or less to provide sufficient contrast for data acquisition in the direct beam. In the case of metallic polycrystals, this condition restricts the applicability of the direct-beam variant to recrystallization or solidification microstructures, which often contain grains with this low level of mosaicity.

Data acquisition in the diffracted beam, on the other hand, allows imaging of grains with slightly higher orientation spreads. Subregions of the grain with slightly different orientations can be imaged by increasing the base tilt integration range. Increasing the integration range leads primarily to longer exposure times and, eventually, to geometrical blurring of the projection images. However, orientation components perpendicular to the diffraction plane will result in angular deviations of the diffracted beams. After propagation, these deviations will manifest as geometric distortions of the projection images, which then no longer correspond to parallel projections of the grain volume. In order to limit the inconsistency of the projection data resulting from this effect, one has to position the detector as close as possible to the sample in case of significant orientation spreads.

Two clear advantages of the diffracted-beam variant are the better signal-to-noise ratio and the ability to work with a reduced number of projections. The latter is possible since one may centre the grain of interest on the rotation axis and thereby limit the lateral projection size. As a consequence, the required number of projections and hence the overall scan acquisition times can be reduced without loss of resolution.

For both variants one has to restrict the energy bandwidth of the incoming radiation. In the direct-beam case this is related to the fact that a bandwidth covering an angular spread larger than the grain orientation spread would lead to a loss of extinction contrast. In the diffracted-beam variant the bandwidth limitation is required in order to avoid distortion of the grain projections, which would lead to inconsistent projection data. When aiming at highest possible spatial resolution, collimation of the synchrotron beam or installation at a high- $\beta$  section of the storage ring will be required to keep typical exposure times short.

### 4.3. Assumptions and limitations

In the discussion of the reconstruction procedure it has been assumed so far that the acquired grain projections correspond to parallel projections of the diffracting grain volume. This is necessarily an over-simplification of the image formation process, the thorough description of which requires formulations of the dynamical theory of X-ray diffraction adapted to the case of deformed crystals (Authier, 2001). A rigorous theoretical treatment being beyond the scope of the current discussion, we will give some semi-quantitative results and estimates of the applicability range deduced from a simple ray optical approximation of the image formation process.

Concerning reconstruction from diffracted-beam data the possible corruption of the projection data related to the presence of orientation spread has already been mentioned. A local misorientation by angle  $\eta$  perpendicular to the diffraction plane will result in a lateral displacement of the diffracted ray on the detector by

$$\Delta x = d \tan 2\theta_{\text{Bragg}} \sin \eta,$$

where  $d$  is the sample-to-detector distance and  $\theta_{\text{Bragg}}$  the Bragg angle of the reflection. Ideally this deviation should be smaller than the pixel size  $p$  of the detector system. Applied to the current case ( $d = 50$  mm,  $\theta_{\text{Bragg}} = 8^\circ$ ,  $p = 2.8$   $\mu\text{m}$ ), this condition restricts the allowable orientation spread to about  $0.01^\circ$ . This estimate considers the worst case of large subgrains with distinct orientations. For the case of a random distribution of small volume elements with orientations fluctuating around the mean orientation, one can expect that consistent reconstructions of the grain outline can still be obtained even if the above-mentioned condition is no longer fulfilled.

Closer inspection of Figs. 2(a) and 2(b) reveals that higher values of the reconstructed 'diffraction power' are observed close to the grain boundary. This, together with the observation of isolated spots exhibiting higher values, clearly indicates that the scattered intensity deviates from a linear relationship with respect to crystal thickness. Primary extinction, and a contrast mechanism known as 'direct image', are at the origin of the observed image contrasts. Distorted regions of the crystal in the vicinity of the inclusions exhibit an effective misorientation that is large enough to allow different wavelengths contributing to the local, integrated intensity. Under the assumption of spherical symmetry of the displacement field associated with the inclusions, this contribution will be roughly constant during sample rotation and can therefore explain the distinct substructure in the tomographic reconstructions (Fig. 2). Owing to the above-mentioned deviation from the linear relationship the recorded projections do not strictly correspond to projections of the grain volume, as would for example be required for a quantitative tomographic reconstruction of the local X-ray attenuation coefficient (including coherent scattering) in the direct-beam case. Note that by changing the imaging conditions such that the grain diameter becomes equal to or smaller than about one-third of the Pendellösung length, one would approach the limit of

kinematical scattering, in which case the direct image contrast would disappear and quantitative reconstructions of the X-ray attenuation coefficient could be obtained.

In unfavourable cases, effects like re-absorption and secondary extinction of the diffracted beam have to be taken into account in the analysis procedure, since both effects can affect the consistency of projections acquired in the diffracted beam. Given the smooth sample outline and the grain position, no significant changes in absorption across the diffracted beam were observed in the current case. Apart from background subtraction and normalization to a constant integrated intensity, no correction was applied to the diffracted-beam projection images. However, knowing the three-dimensional attenuation coefficient distribution from the direct-beam reconstruction one could calculate the attenuation along the diffracted beams and correct the intensity distribution in a quantitative way. Given the small number of grains in the current sample, secondary extinction was not an issue here. In the case of polycrystals with a large number of randomly oriented grains, occasionally occurring extinction events would be averaged out given the large number of projection images available. In the case of a material exhibiting strong texture, overlapping grain contrasts in the direct beam and inconsistent intensity distributions can be expected to limit the quality of the reconstructions.

#### 4.4. Extensions

For the current proof-of-principle experiment, a suitable reflection of an arbitrary grain was selected and aligned for diffraction. This alignment procedure is unsatisfactory in the sense that it offers no deterministic way to select directly a particular grain within a given sample volume. Ideally, topotomography should therefore be combined with a polycrystal indexing procedure (Lauridsen *et al.*, 2001) providing access to grain orientations and possibly also the centre of mass positions of the grains. Apart from speeding up the alignment procedure itself this would also open the possibility to image grains in particular regions of interest and/or to characterize small clusters of grains by successive scans.

It will be interesting to explore how far this imaging mode can be adapted to the characterization of grain (sub-) structures such as twins, subgrains, and lamellar or dendritic grain structures. The sensitivity of the topographic image contrast towards long-range strain fields related to such features may potentially reveal structures that cannot be detected by means of conventional absorption and/or phase contrast imaging.

The above-mentioned possibility to work with a reduced number of projections makes the diffracted-beam variant a promising candidate for *in situ* observations. Further optimization of the monochromatic flux (for instance by use of collimating X-ray optics) will allow a reduction of the overall scan acquisition times to the level of 1 min. As a possible application one may think of *in situ* bulk observations of grain boundary–microstructure interactions occurring during dynamic grain coarsening processes such as recrystallization and grain growth.

Last but not least, we mention the possibility to apply the same methodology to the case of neutron imaging. Although limited in flux and spatial resolution, this alternative material probe could be of interest for the case of large-grained polycrystals (> 1 mm grain size) containing elements with high atomic numbers (to strong X-ray attenuation).

## 5. Conclusions

The principle of topotomographic imaging has been used to analyse the three-dimensional shape and substructure of one individual, embedded grain in the bulk of a polycrystalline sample with high spatial resolution. Data acquisition can be performed either in the direct or in the diffracted beam. In the direct-beam case, the shape of undeformed grains may be visualized simultaneously with the materials microstructure as determined from conventional X-ray absorption and/or phase contrast tomography. The contrast mechanism involved is sensitive to orientation changes and strain fields inside the crystal and can reveal the presence of second-phase inclusions smaller than the actual resolution limit of the detector system.

Given a tomographic imaging setup with the required mechanical degrees of freedom, the technique can be implemented on any second- or third-generation synchrotron imaging beamline.

## APPENDIX A

If the grain orientations are not known *a priori*, the following procedure can be used to establish alignment for a randomly selected grain (see also Fig. 1.)

### A1. Coarse alignment procedure (grain orientation unknown)

(1) Perform a conventional alignment of the tomographic setup: rotation axis parallel to the columns of the detector system and perpendicular to the beam axis (base tilt  $T_0 = 0$ ), and sample centred on the rotation axis.

(2) Position the detector a few millimetres behind and slightly above the sample in order to capture diffraction spots from low-order reflections, which occasionally appear when the sample is turned around the rotation axis.

(3) Given a suitable diffraction spot, the corresponding diffraction vector is determined by tracking the diffracted-beam direction *via* a small detector movement along the beam axis.

(4) Calculate the sample goniometer tilts required to align the diffraction vector parallel to the rotation axis. [Since the goniometer tilts only cover a limited angular range, steps 2–4 may have to be repeated a few times until a suitable reflection (requiring only small tilt angles) has been found.]

(5) Apply sample tilts and proceed with fine tuning.

### A2. Final alignment procedure

Once a reflection has been pre-aligned, the following fine-tuning procedure should rapidly lead to the required accuracy in alignment of the diffraction vector.

(1) Set base tilt  $T0$  to the nominal Bragg angle of the reflection.

(2) Rotate the sample into position  $\omega_0$ , where the tilt axes of  $T0$  and  $T1$  are collinear (perpendicular to the plane spanned by the beam and the rotation axis).

(3) Find optimum positions  $\tau_{1,2}$  for tilt  $T1$  at  $\omega_1 = \omega_0$  and at  $\omega_2 = \omega_0 + 180$ , respectively.

(4) Move  $T1$  to position  $(\tau_1 + \tau_2)/2$  and correct base tilt value  $T0$  by  $(\tau_1 - \tau_2)/2$ .

(5) Rotate the sample by  $90^\circ$  and adjust  $T2$  to the optimum position.

(6) Check that the reflection is now visible for any  $\omega$  setting of the rotation (otherwise repeat steps 3–5).

(7) Determine the integration range for base tilt  $T0$ , required to illuminate the entire grain.

The authors would like to thank P. Bernard for technical support and G. Berruyer and P. Cloetens for assistance in implementing the scanning procedure. This work was supported by the Danish National Research Foundation, by the EU programme TotalCryst and by the Danish National Science Research Council (*via* Dansync).

## References

- Authier, A. (2001). *Dynamical Theory of X-ray Diffraction*. New York: Oxford University Press.
- Barnard, J. S., Sharp, J., Tong, J. R. & Midgley, P. A. (2006). *Science*, **313**, 319.
- Cloetens, P., Pateyron-Salomé, M., Buffiere, J. Y., Peix, G., Baruchel, J., Peyrin, F. & Schlenker, M. (1997). *J. Appl. Phys.* **81**, 9.
- Kak, A. C. & Slaney, M. (1988). *Principles of Computerized Tomographic Imaging*. New York: IEEE Press.
- Kvardakov, V. V., Podurets, K. M., Schetinkin, S. A., Baruchel, J., Härtwig, J. & Schlenker, M. (2007). *Nucl. Instrum. Methods Phys. Res. A*. In the press.
- Larson, B. C., Yang, W., Ice, G. E., Budai, J. D. & Tischler, J. Z. (2002). *Nature (London)*, **415**, 887–890.
- Lauridsen, E. M., Schmidt, S., Suter, R. M. & Poulsen, H. F. (2001). *J. Appl. Cryst.* **34**, 744–750.
- Ludwig, W., Cloetens, P., Härtwig, J., Baruchel, J., Hamelin, B. & Bastie, P. (2001). *J. Appl. Cryst.* **34**, 602–607.
- Poulsen, H. F. (2004). *Three-Dimensional X-ray Diffraction Microscopy. Mapping Polycrystals and their Dynamics*, Springer Tracts in Modern Physics. Berlin: Springer.
- Servidori, M., Cembali, F. & Milita, S. (2001). *Appl. Phys. A*, **73**, 74–82.
- Snigirev, A., Snigireva, I., Kohn, V., Kuznetsov, S. & Schelokov, I. (1995). *Rev. Sci. Instrum.* **66**, 5486–5492.
- Tanner, B. K. (1976). *X-ray Diffraction Topography*. Oxford: Pergamon Press.